

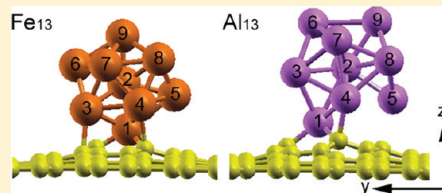
DFT Studies on the Interaction of Defective Graphene-Supported Fe and Al Nanoparticles

Dong-Hee Lim, Ana Suarez Negreira, and Jennifer Wilcox*

Department of Energy Resources Engineering, Stanford University, 367 Panama Street, Green Earth Sciences, Stanford, California 94305-2220, United States

 Supporting Information

ABSTRACT: The structural, electronic, and magnetic properties of Fe_{13} and Al_{13} nanoparticles adsorbed on monovacancy defective graphene have been determined using density functional theory with the generalized gradient approximation (GGA). Graphene vacancies are used as anchoring points for these pure metal nanoparticles, ensuring their isolated stability on the surface, thereby maximizing their catalytic reactivity through the availability of undercoordinated surface sites along with a high surface area. The results of this work indicate that the strong binding of Fe_{13} and Al_{13} nanoparticles on defective graphene (-6.98 and -3.84 eV in adsorption energy, respectively) is due to strong hybridization of the nanoparticles with the sp^2 dangling bonds of neighboring carbons near the vacancy. Charge difference and Bader charge analyses of the Fe_{13} and Al_{13} adsorbed systems suggest that charge redistribution of defective graphene occurs to a greater extent in the Fe_{13} system than in the Al_{13} system due to the strongly hybridized Fe_{13} d-states with the monovacancy defective site of graphene. For the Fe_{13} nanoparticle, upon adsorption its d-band center shifts closer to the Fermi level from -1.28 to -1.13 eV, indicating a potential increase in the catalytic reactivity associated with the graphene surface.



1. INTRODUCTION

Graphene is one planar sheet of sp^2 -bonded carbon atoms arranged in a hexagonal lattice and is the basis of carbon nanotubes.¹ The importance of graphene sheets has been demonstrated in a variety of applications including high electron mobility, and the enhancement of mechanical and electrical properties of composite materials.² The presence of defects on the graphene structure due to carbon vacancies influences the chemical and physical characteristics of graphene³ since it generates nonequivalent carbon atoms on the surface. Defect sites present higher reactivity for adsorption, which makes chemical functionalization an easy method to detect imperfections on graphene.⁴ Defective graphene where carbon atoms are missing can be obtained, for example, during generation of functionalized single graphene sheets (FGSs) from the thermal expansion of graphite oxide (GO).⁵ Monovacancies, multivacancies, pentagon–heptagon pairs, and adatoms are predicted as typical stable graphene defects.⁶ Tight-binding molecular dynamics (TBMD) simulations predicted that two single vacancies coalesce into a double vacancy 5–8–5 defect where two carbon atoms are missing, leaving a surface with two pentagonal rings and one octagonal ring.⁷

The defect sites in graphene can be used as starting points for the growth of nanoparticles. A previous experimental study suggests that the presence of defects on graphene substrates allows for controlled morphology of iron nanoparticles.⁸ These graphene-supported nanocrystals may enhance the rate of electron transport while influencing the structural stability of the material, both effects potentially leading to enhanced surface reactivity.⁹

Nanoparticles composed of Fe and Al are considered in the current study with specific focus on the modification of their mechanical and electronic properties from bulk to nanoparticle scale, similar to previous investigations,¹⁰ but with special interest to catalysis applications. Changes in the lattice constant, surface stress, and surface energy associated with nanoparticle size¹⁰ may influence their surface reactivity. For example, in the case of Fe nanoparticles, reactivity with hydrogen and binding energies of ammonia and water significantly change depending on the Fe_n cluster size (e.g., $n \leq 23$).¹¹ The magnetic moments of Fe_n clusters also vary remarkably depending on the size of the Fe clusters^{12–14} in addition to the environment in which they are adsorbed. The effect of the substrate was shown in previous studies of Fe clusters deposited on a $\text{MgO}(111)$ substrate¹⁵ and embedded in a Co matrix.¹⁶ Supported Al nanoparticles are of interest to the combustion community for fuel enhancement with regard to combustion rates and combustion exothermicity of energetic materials, for instance. Rocket propellants can be enhanced by the addition of Al nanoparticles within a given fuel.^{17,18} Additionally, it is interesting to study the fundamental differences between the mechanisms of nanoparticle binding in the case of Al versus Fe, to specifically outline the role that the d electrons of Fe may play in enhancing nanoparticle sorption and/or nanoparticle surface chemical reactivity.

Experimental work carried out by Sakuri et al.¹⁹ indicate that transition-metal clusters (Fe, Ti, Zr, Nb, and Ta) with “magic

Received: February 9, 2011

Revised: March 21, 2011

Published: April 18, 2011

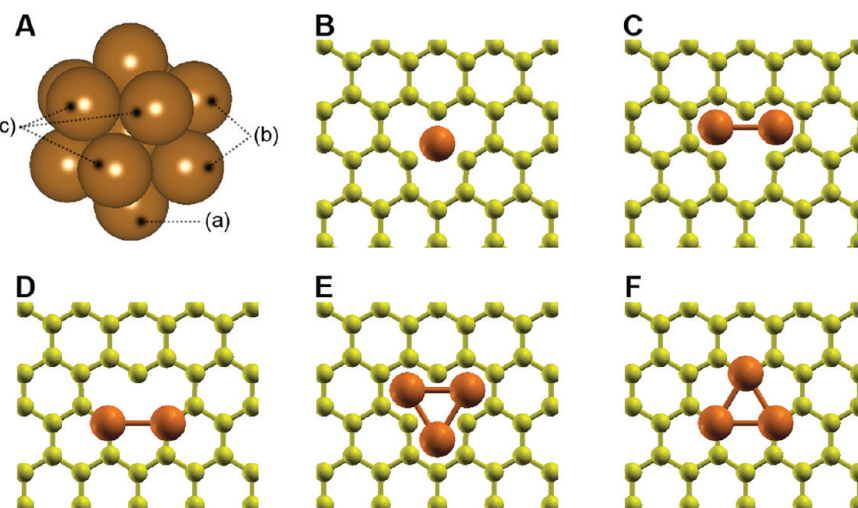


Figure 1. Five different initial adsorption modes of nanoparticles (NPs) on defective graphene with a monovacancy. (A) Icosahedral symmetry of NPs. (B) Atop-bridge mode. (C) Bridge–bridge mode. (D) Bridge-atop mode. (E) Triple-bridge mode. (F) Triple-atop mode. In panel A, (a) indicates adsorbed atom for mode B, (b) indicates adsorbed atoms for modes C and D, and (c) indicates adsorbed atoms for modes E and F.

numbers” $n^{19,20}$ such that $n = 7, 13$, and 15 atoms in a given cluster, have a higher geometric and/or electronic stability than other cluster sizes. A previous DFT study¹² reports that Fe clusters may also have magic numbers of $8, 10, 13$, and 15 . For the current study, $n = 13$ has been chosen with an icosahedral configuration to likely have the most energetically favorable structure of the Fe_{13} cluster.^{11,12,21,22} Clusters of Al_{13} with the icosahedral symmetry have also been shown to exhibit enhanced stability.¹⁰

Previous studies focused on understanding functionalized or doped graphene surfaces,^{23,24} and investigations of supported Fe and Al nanoparticles have been limited to perfect graphene sheets. The goal of the current study is to use graphene vacancies as anchoring points for the pure Fe and Al nanoparticles, ensuring their isolated stability on the surface, thereby maximizing their catalytic reactivity through maximum availability of undercoordinated surface sites along with a high surface area.

It is well-known that Fe and Al are easily oxidized materials and that even minimally oxidizing conditions will lead to their oxidized forms. The current study focuses specifically on the pure metal nanoparticles of Fe and Al, but future work will consider systems in which the outer metal atoms of the nanoparticle cluster are bound to oxygen sourced from molecular oxygen in equilibrium with the surface.

2. COMPUTATIONAL METHODOLOGY

Density functional theory calculations were performed using the Vienna ab initio Simulation Package (VASP)^{25–28} with the projector-augmented wave (PAW)^{29,30} method to calculate the electronic and atomic structures and energies of Fe and Al nanoparticle–graphene systems. Electron exchange-correlation functionals were represented with the generalized gradient approximation (GGA), and the model of Perdew, Burke, and Ernzerhof (PBE)³¹ was used for the nonlocal corrections. For the Fe nanoparticle and defective graphene, the spin-polarized GGA–PBE was used. An orthorhombic supercell of $19.74 \times 17.10 \times 32.01 \text{ \AA}$ with periodic boundary conditions was used for the nanoparticle–graphene systems. The nanoparticle–graphene system was separated from its periodic images in the

z -direction by a vacuum space of 25.5 \AA . To compensate for the dipole moment perpendicular to the surface, a dipole moment correction was incorporated^{32,33} and tested but not included in the adsorption calculations due to its negligible effect on adsorption energy. A kinetic energy cutoff of 400 eV was used with a plane-wave basis set. The integration of the Brillouin zone was conducted using a $2 \times 2 \times 1$ Monkhorst–Pack grid³⁴ with the Γ -point included and first-order Methfessel–Paxton smearing³⁵ with a width of 0.1 eV . All atoms were fully relaxed and optimized until the forces were reduced below $1 \times 10^{-2} \text{ eV}/\text{\AA}$.

The supercell used for graphene consists of 127 carbon atoms with a single carbon atom vacancy at the center. The geometry optimization of graphene was carried out using the same condition as was used in the nanoparticle–graphene systems but with a Gaussian smearing width of 0.2 eV . This is a relatively larger smearing width but is traditionally used in DFT studies of graphene³⁶ and graphite³⁷ and provides a reasonable magnetic moment of defective graphene compared to previous DFT studies in which smaller smearing widths were used.^{38,39} The formation energy for the monovacancy ($E_{\text{formation}}$) is calculated as:

$$E_{\text{formation}} = E_{\text{vac}} - \frac{n-1}{n} E_{\text{perfect}} \quad (1)$$

where E_{vac} and E_{perfect} are the total energies of defective and perfect graphene, respectively. n is the number of atoms in the perfect graphene.

The interactions between defective graphene and Fe_{13} and Al_{13} nanoparticles with icosahedral symmetry^{13,21} were investigated. Beginning with the bulk lattice constants of each system (2.83 \AA for bulk bcc Fe and 4.04 \AA for bulk fcc Al), isolated Fe_{13} and Al_{13} nanoparticles were optimized in a 25.4 \AA cubic supercell. The Brillouin zone integration was carried out for the Γ -point only. In the case of Fe, the ferromagnetic spin state of Fe_{13} was employed because the ferromagnetic spin state (total spin magnetic moment of $44 \mu_B$) is known to have a lower energy compared to the anti-ferromagnetic spin state (total spin magnetic moment of $34 \mu_B$).^{13,21}

Five different initial adsorption configurations of the nanoparticles were considered in the current study and are dependent on the number of nanoparticle atoms that adsorb on the vacancy site of graphene as indicated in Figure 1. The adsorption energy

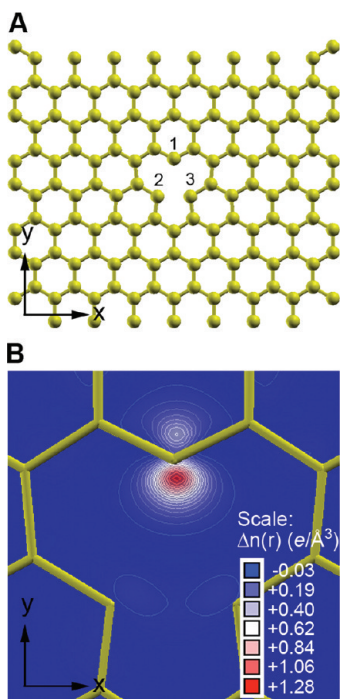


Figure 2. (A) Optimized structure of a monovacancy defect graphene (127 carbon atoms) and (B) its spin density at the vacancy site (unit: $e/\text{\AA}^3$).

(E_{ads}) per nanoparticle is calculated as:

$$E_{\text{ads}} = \frac{1}{N_{\text{cluster}}} (E_{\text{surf+cluster}} - E_{\text{surf}} - N_{\text{cluster}} \times E_{\text{cluster}}) \quad (2)$$

where N_{cluster} is the number of nanoparticles in the model system. $E_{\text{surf+cluster}}$, E_{surf} , and E_{cluster} are the total energies of defective graphene with adsorbed nanoparticle, bare defective graphene, and gas-phase nanoparticles. A negative adsorption energy indicates that adsorption is exothermic (stable) with respect to the free nanoparticle cluster.

The charge difference density ($\Delta n(\mathbf{r})$) plots were obtained by subtracting the charge densities of the separated nanoparticles and defective graphene from the charge density of the Fe and Al systems as follows:

$$\Delta n(\mathbf{r}) = n_{\text{surf+cluster}}(\mathbf{r}) - [n_{\text{surf}}(\mathbf{r}) + n_{\text{cluster}}(\mathbf{r})] \quad (3)$$

where $n_{\text{surf+cluster}}(\mathbf{r})$, $n_{\text{surf}}(\mathbf{r})$, and $n_{\text{cluster}}(\mathbf{r})$ are the electron charge distributions of the defective graphene with adsorbed nanoparticles, isolated defective graphene, and isolated nanoparticles, respectively. The source of the isolated nanoparticle and defective graphene structures used for the charge difference density calculations have been directly obtained from the optimized structures of the bound systems, rather than the optimized free NP and graphene systems. The density plots have been created using the XCrySDen graphical package.⁴⁰

To quantitatively compare transferred charges between the Fe and Al nanoparticles and defective graphene, a Bader charge analysis^{41–43} has also been carried out. The optimized geometry of the Fe and Al systems, isolated nanoparticles, and defective graphene are kept fixed for the Bader charge analysis. For improved accuracy, the structures with fixed geometries have been calculated with a second finer fast fourier transform (FFT)-mesh 4 times that used in the adsorption calculations.

3. RESULTS AND DISCUSSION

A. Geometry and Magnetism of Defective Graphene with Monovacancy. Upon relaxation of a monovacancy defective graphene (127 carbon atoms) surface, the neighboring carbon atoms near the vacancy form a pentagonal-like ring as shown in Figure 2A. Due to the single carbon vacancy that results in a carbon–carbon bond cleavage, the neighboring carbon atoms near the vacancy (C1, C2, and C3 as shown in Figure 2A) have sp^2 dangling bonds.^{38,39,44} This agrees well with other DFT studies of defective graphene in that the vacancy site undergoes Jahn–Teller distortion,^{38,39,44–46} in which the C2 and C3 dangling bonds are reconstructed because of the single carbon vacancy. The distance between C2 and C3 atoms contracts from the standard length of 2.47 Å in perfect graphene to 2.04 Å in monovacancy defective graphene, with the C1 atom displaced by a distance, $\Delta z = 0.12$ Å out-of-plane. This phenomena has been documented in previous studies with C1 out-of-plane displacements,⁴⁵ Δz , of 0.18 Å³⁸ and 0.47 Å.⁴⁵ The distortion can be explained on account of the weak covalent C–C bond between the C2 and C3 atoms that repel the C1 atom, resulting in the out-of-plane distortion. This geometric distortion also agrees well with other DFT studies of defective graphene with the monovacancy.^{38,44,45} However, some DFT studies^{39,45,46} show that the C2–C3 length becomes longer after geometry optimization of the defective graphene and may be attributed to a local minimum of the symmetric D_{3h} vacancy of graphene where only in-plane reconstruction of the C2 and C3 atoms occurs without the out-of-plane distortion of the C1 atom.⁴⁵ El-Barbary et al.⁴⁵ show that the defective graphene with the distorted vacancy yields a reduced energy of around 0.2 eV compared to the symmetric vacancy in $C_{120}H_{27}$ systems. The formation energy for the monovacancy site in graphene is approximately 7.7 eV of the current study, which agrees well with the experimental value of 7.0 ± 0.5 eV⁴⁷ and with the previous DFT values of 7.7³⁸ and 7.8 eV.³⁹

Perfect graphene is nonmagnetic, but the presence of the monovacancy in graphene induces magnetism by breaking the symmetry in the π -electron system of graphene.^{38,39,44,48} We predict that the magnetic moment of the defective graphene with monovacancy is $1.22 \mu_B$. The study carried out by Ma et al.³⁸ resulted in a calculated magnetic moment of the monovacancy of $1.04 \mu_B$, and they found from spin density analysis that the magnetic moment is attributed to the remaining unsaturated bond (C1) after the formation of the C2–C3 bond in the pentagon shape.^{38,44} We also confirm from the spin density analysis that the unsaturated sp^2 dangling bond at C1 significantly contributes to the total magnetic moment of defective graphene as shown in Figure 2B. Depending on the packing distance of monovacancies, the magnetic moment varies from $1.15 \mu_B$ for the smallest distance to $1.45–1.53 \mu_B$ for greater distances.⁴⁴ The structural and magnetic property agreement of the monovacancy site of defective graphene between previous investigations available in the literature and in the current study validates the computational parameters chosen for the defective graphene model of the current study.

B. Adsorption of Fe_{13} and Al_{13} Nanoparticles on Defective Graphene. The geometries of isolated Fe_{13} and Al_{13} nanoparticles were optimized in the gas phase with the cluster radii defined as the distance from the atom at the center of a nanoparticle to the outer edge atoms. The cluster radii are 2.40 and 2.67 Å for Fe_{13} and Al_{13} clusters, respectively. These results are

Table 1. Adsorption Energy (E_{ads}) and Average Cluster Radius (r_{avg} with standard deviation (SD) and maximum, minimum values) of Fe_{13} and Al_{13} Nanoparticles, and Bond Lengths of Neighboring Carbon Atoms ($d_{\text{C}12}/d_{\text{C}23}$) Near the Vacancy of Defective Graphene^a

| | Fe ₁₃ system | | | Al ₁₃ system | | |
|--------------------|-------------------------|---|-------------------------------------|-------------------------|---|-------------------------------------|
| | E_{ads} (eV) | r_{avg} ($\pm \text{SD}$) (max, min) (Å) | $d_{\text{C}12}/d_{\text{C}23}$ (Å) | E_{ads} (eV) | r_{avg} ($\pm \text{SD}$) (max, min) (Å) | $d_{\text{C}12}/d_{\text{C}23}$ (Å) |
| (A) nanoparticle | — | 2.40 | — | — | 2.67 | — |
| (B) A–B mode | −6.98 | 2.39 (± 0.09) (2.50, 2.24) | 2.72/2.70 | −3.84 | 2.72 (± 0.10) (2.92, 2.60) | 2.87/2.95 |
| (C) B–B mode | −4.62 | 2.39 (± 0.07) (2.47, 2.29) | 2.68/2.78 | −1.83 | 2.67 (± 0.05) (2.71, 2.59) | 2.58/2.82 |
| (D) B–A mode | −4.05 | 2.38 (± 0.03) (2.42, 2.34) | 2.75/2.40 | −1.84 | 2.68 (± 0.04) (2.73, 2.61) | 2.58/2.83 |
| (E) T–B mode | −4.57 | 2.39 (± 0.05) (2.47, 2.32) | 2.63/2.61 | −1.87 | 2.69 (± 0.05) (2.79, 2.63) | 2.77/2.77 |
| (F) T–A mode | −3.89 | 2.39 (± 0.05) (2.49, 2.36) | 2.65/2.59 | −1.92 | 2.67 (± 0.04) (2.73, 2.61) | 2.82/2.82 |
| defective graphene | — | — | 2.57/2.04 | — | — | 2.57/2.04 |

^a Symbols A–F indicate adsorption configurations as labeled in Figure 1.

consistent with previous DFT studies of Fe_{13} (2.40 Å)⁴⁹ and Al_{13} clusters (2.76 Å).¹⁰ We confirm that the total magnetic moment of the ferromagnetic spin state of the icosahedral Fe_{13} cluster is $44 \mu_B$ in agreement with other DFT studies.^{13,21}

Among the five different adsorption configurations tested as shown in Figure 1, the atop-bridge mode (A–B mode) where one nanoparticle edge atom interacts with three sp^2 dangling bonds of carbon at the vacancy site shows exceptional stability compared to the other modes where two or three nanoparticle atoms are placed near the vacancy site. The details of the relative stabilities and adsorption energies associated with the various configurations are available in Table 1. The adsorption energies for the most stable Fe_{13} and Al_{13} nanoparticles are found to be −6.98 and −3.84 eV, respectively, when the dipole moment correction is not applied. The effect of the dipole moment correction is negligible and in the case of the most stable adsorption configuration of the Fe system, the correction causes the adsorption energy to change by approximately 3.5 meV (note this comparison was made with less strict geometry convergence criterion than described in Computational Methodology, i.e., total energy change upon the relaxation of the electronic degrees of freedom less than 10^{-4} eV). We also calculated the A–B adsorption modes of the Fe and Al nanoparticles at the center of a hexagonal lattice of perfect graphene. The Fe_{13} nanoparticle has an adsorption energy of −0.89 eV on perfect graphene. On the perfect graphene system, the second-layer Fe atoms contract toward the surface carbon atoms with the nanoparticle tilting into the surface. The Al_{13} nanoparticle on the perfect graphene surface is barely stable with an adsorption energy of −0.13 eV. Because of the monovacancy, Fe_{13} and Al_{13} nanoparticle adsorption is significantly enhanced on graphene. The strong interaction between the nanoparticles and the carbon-vacancy defect in graphene is attributed to the sp^2 dangling bond formed at the three neighboring carbon atoms near the vacancy⁵⁰ due to the carbon–carbon bond cleavage.^{38,39,44} These relatively strong adsorption energies are comparable with enhanced adsorption energies of Pt_4 and Au_8 cluster binding at a monovacancy defect site of graphene, increasing from −1.4 to −7.7 eV for Pt_4 and from −0.71 to −1.56 eV for Au_8 .⁵⁰ The adsorption energy of the Au_6 cluster also is enhanced from −0.3 eV on perfect graphene up to −2.6 eV on defective graphene with a monovacancy.⁵¹

Figure 3 shows top and side views of the most stable Fe_{13} and Al_{13} nanoparticle configurations (A–B mode) on the monovacancy defect site of graphene. The adsorbed configurations of

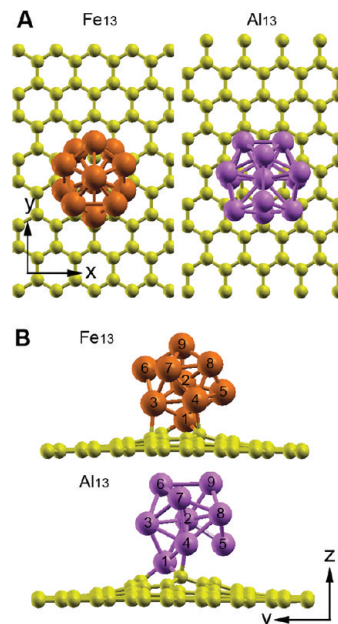


Figure 3. (A) Top view and (B) side view of adsorbed Fe_{13} and Al_{13} nanoparticles on the defect site of graphene.

the rest modes are shown in Supporting Information Figures S1 and S2. Upon adsorption, both geometries of the adsorbed nanoparticles and the initially planar surface of defective graphene are distorted and strongly reconstructed. The Fe_{13} and Al_{13} cluster radii change, ranging from 2.24 to 2.50 Å (−6.6–4.1% change) and 2.60 to 2.92 Å (−2.8–9.4% change), respectively. The Fe_{13} nanoparticle contracts vertically with a horizontal expansion, while the Al_{13} nanoparticle expands in both directions. Comparing the five adsorption configurations of each nanoparticle, the stronger nanoparticle–surface interaction leads to greater distortion. As can be seen in Table 1, the greater deviation from the average cluster radius correlates with increased nanoparticle distortion.

The initially planar surface of defective graphene strongly reconstructs with relaxation normal to the surface (i.e., in the z -direction), especially near the defect site as shown in Figure 3B. The height of the carbon atoms near the defect site increases up to 1.09 and 1.48 Å for Fe_{13} and Al_{13} systems, respectively. Figure 4 shows that the elevated height of the carbon atoms is the highest at

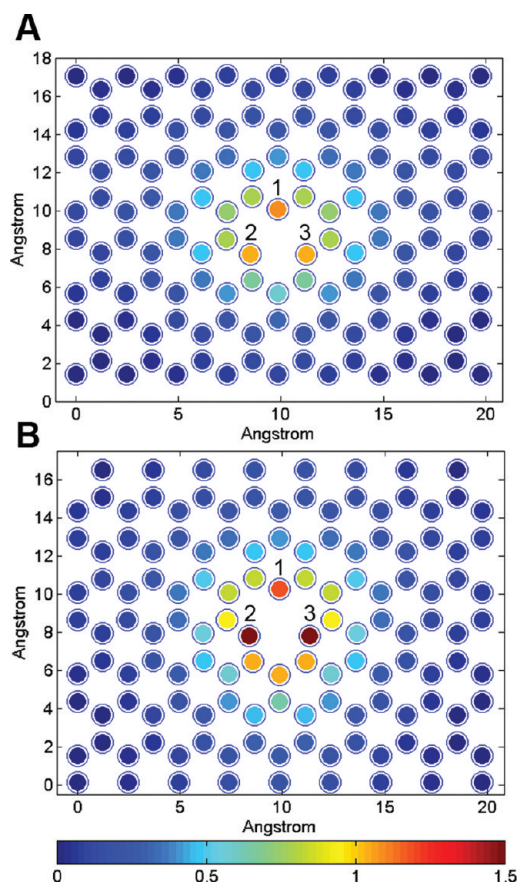


Figure 4. Elevated height (in units of Å) of carbon atoms after Fe_{13} (A) and Al_{13} (B) nanoparticle adsorption.

the nearest benzene rings near the adsorption site (defect site) and decreases with respect to the distance from the adsorption site. This elevation of carbon atoms upon adsorption of adsorbates is a common phenomenon of defect sites of graphene.^{39,50,52–54} The average distances between the directly bound atom of the nanoparticle (i.e., Fe1 or Al1) and the three neighboring carbon atoms nearest the monovacancy of the Fe_{13} and Al_{13} systems are 1.83 and 1.95 Å, respectively. The increase in carbon's height and the longer average distance of Al1–C1,2,3 compared to the Fe system are due to the larger atomic radius of Al compared to Fe. These observations are in agreement with a previous DFT study in which Fe and Al atoms are adsorbed on perfect graphene with reports of a greater distance of Al–C compared to Fe–C.⁵⁵ On the other hand, lateral relaxation of the graphene lattice is not significant compared to the relaxation normal to the surface. Due to nanoparticle adsorption, the weak covalent C2–C3 bond, with an original distance of 2.04 Å, is broken and each C2 and C3 atom interacts directly with atom 1 (Figure 3) of the nanoparticle. This is supported by the elongated C2–C3 distances of 2.70 and 2.95 Å for the Fe and Al systems, respectively. The carbon–carbon bond lengths at the three-pentagon perimeter near the vacancy site increase by up to 0.08 Å and 0.07 Å for the Fe and Al systems, respectively, with the exception of the direct bonds with C2 and C3 atoms that decrease due to the elongation of the C2–C3 bond. These geometry distortions of both the nanoparticles and defective graphene demonstrate that the Fe_{13} and Al_{13} nanoparticles interact strongly with the defect site of graphene.

One interesting observation regarding the nanoparticle adsorption is that the Fe_{13} and Al_{13} nanoparticles are tilted toward opposite directions of each other as shown in Figure 3B. This is caused by different initial positions of the nanoparticle atoms on the defect site of graphene due to different atomic radii, which determines distance between Fe or Al and carbon atoms near the monovacancy. Before adsorption, the average distances between Fe3 and Al3 and their nearest pentagon-shaped carbon atoms near the C1s atom are 3.26 and 3.33 Å, respectively. Similarly, the average distances between the Fe4 and Al4 atoms and their nearest hexagon-shaped carbon atoms near the C2 atoms are 3.27 and 3.25 Å, respectively. The shorter initial distance of the Fe3–pentagon and Al4–hexagon areas initiates a stronger interaction near the C1 atom for the Fe_{13} nanoparticle and near C2 and C3 atoms for the Al_{13} nanoparticles, resulting in opposite tilting directions of each other. Different adsorption configurations due to different initial positions of nanoparticles in the A–B mode are shown in Supporting Information Figure S3.

C. Projected Density of States (PDOS) of Fe_{13} and Al_{13} Nanoparticles on Defective Graphene. The projected density of states (PDOS) has been analyzed for the valence electrons of the isolated nanoparticles (Fe_{13} and Al_{13}) and defective graphene in addition to the adsorbed complexes. The PDOS analyses are useful for understanding the details of the interaction between the Fe_{13} and Al_{13} nanoparticles and defective graphene. The PDOS is calculated by projecting the electron wave functions onto spherical harmonics centered on each type of metal atom.

Figure 5 shows plots of the PDOS of the d-states of the Fe_{13} nanoparticle (A) before and (B) after adsorption, the p-states of the Al_{13} nanoparticle (C) before and (D) after adsorption, and the p-states of defective graphene (C1 and C2 of Figure 2A) (E) before and (F) after adsorption, where the Fermi energy is referenced at 0 eV. While Fe and Al atoms in the isolated nanoparticles show narrow and sharp bands, Fe and Al atoms in the adsorbed nanoparticles represent broader and strongly modified bands ranging from –7 to 3 eV and from –10 to 5.5 eV, respectively. For Fe, Figure 5B shows strong hybridization between Fe 3d-states and defective graphene states, indicating covalent bonding between Fe and C atoms.⁵⁵ For Al, Figure 5D reveals that 3s- and 3p-states of Al broaden noticeably and shift to lower energy levels due to the Al-defective graphene interaction. For example, the 3s-state of Al2 (the center atom of Al_{13}) at –8.7 and –2.3 eV relative to E_F before adsorption appears to split and hybridize with the defective graphene at energies of –9.3, –3.5, and 2.5–5.5 eV relative to E_F after adsorption. These broadened and strongly modified states of Fe and Al indicate a strong hybridization of the nanoparticles with the sp^2 dangling bonds of carbon.

Figure 5E shows that the spin states of the p orbital of the C1 atom near the vacancy split at approximately the Fermi energy leading to spin-polarized states and resulting in asymmetry of the spin-up and spin-down states. However, the p orbitals of the C2 and C3 atoms are symmetric, indicating that the total magnetic moment caused by the monovacancy is localized at the C1 atom, rather than at the C2 or C3 atoms. The spin density analysis of defective graphene in Figure 2B agrees with the PDOS analysis of C1 and C2 atoms in Figure 5E. Yang et al.⁴⁶ also reported similar results of the PDOS of the C1, C2, and C3 atoms near the vacancy, but they concluded that the C2 and C3 atoms give rise to the splitting of the spin states, leading to the spin-polarized states. This discrepancy may be attributed to different optimized structures of monovacancy graphene between Yang et al.'s and

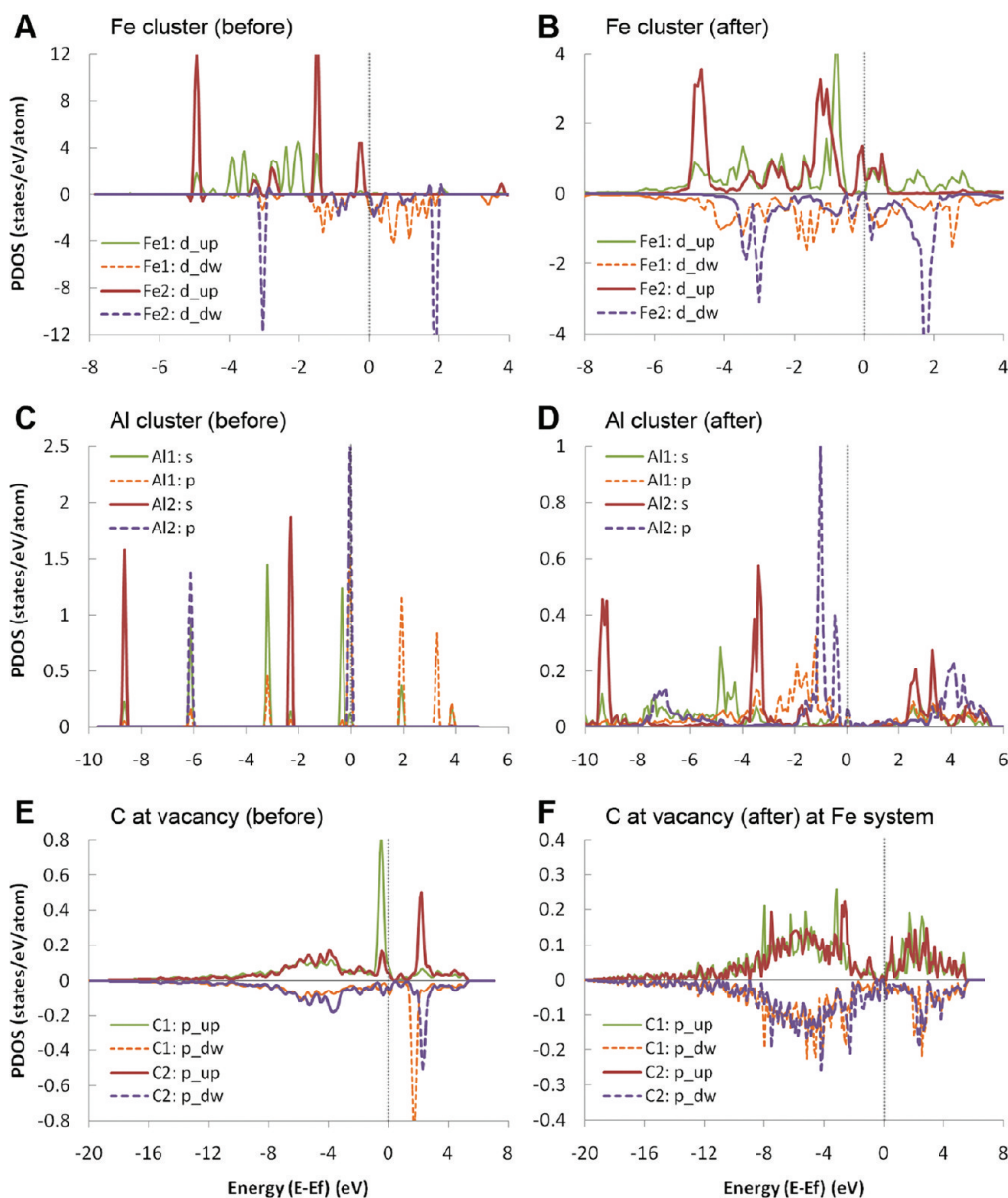


Figure 5. Projected density of states (PDOS) for nanoparticles and defective graphene before and after adsorption. (A and B) d-state of Fe_{13} before and after adsorption, respectively. (C and D) p-state of Al_{13} before and after adsorption, respectively. (E and F) p-state of the monovacancy defect graphene before and after adsorption, respectively. Subscripts 1 and 2 for Fe and Al represent the bound Fe or Al atom at the vacancy site and the centered Fe or Al atom in the nanoparticles, respectively (as labeled in Figure 3B). C1 and C2 atoms represent the C atoms neighboring the vacancy as depicted in Figure 2A. The Fermi energy is referenced at 0 eV.

the current study. While Yang et al.'s study considers the symmetric D_{3h} vacancy of graphene with a C2–C3 bond of 2.67 Å, the structure of the current work has a distorted vacancy site with a C2–C3 bond distance of 2.04 Å, as discussed previously. In the distorted vacancy of monovacancy graphene, a localized magnetic moment is strongly shown at the C1 atom as shown in previous studies.^{38,44} Strong unoccupied bands above the Fermi level in Figure 5E due to the sp^2 dangling bonds of carbon are filled and shifted to below the Fermi level in Figure 5F after adsorption of the Fe_{13} nanoparticle. The same phenomenon is shown in the case of Al_{13} adsorption on the vacancy site of graphene, demonstrating that the valence orbitals of the Fe and Al nanoparticle strongly interact with the graphene surface.

D. Charge Transfer between Nanoparticles and Defective Graphene. To understand enhanced adsorption of Fe_{13} and Al_{13} nanoparticles on defective graphene, we conduct charge difference density and Bader charge analyses.^{41–43} Figure 6 displays the charge difference density, i.e., the difference between the density of the nanoparticle-defective graphene system and its separated constituents (adsorbate and substrate). The red color represents charge accumulation, while the blue color charge depletion. In Figure 6, strong charge accumulation is observed at the neighboring carbon atoms (C1, C2, and C3) near the vacancy due to the interaction between the sp^2 dangling bonds of carbon and the nanoparticles. This indicates that both Fe_{13} and Al_{13} nanoparticles donate electrons to defective graphene, in

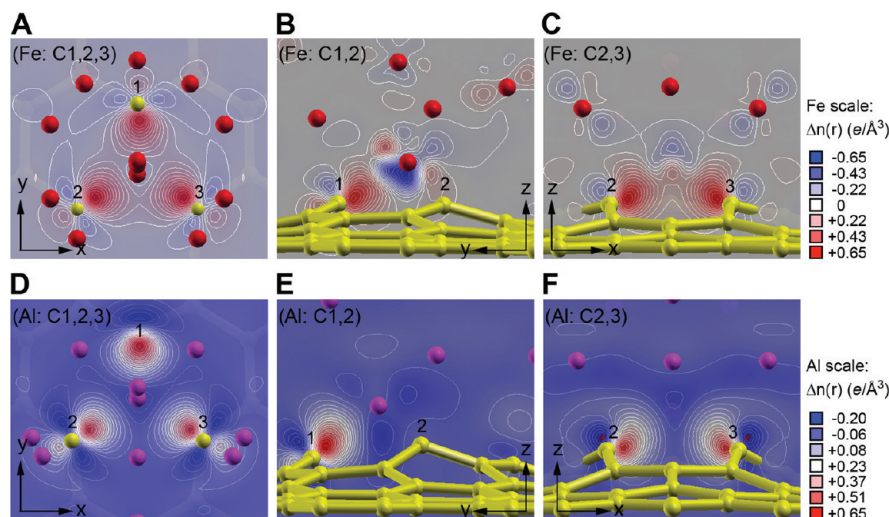


Figure 6. Charge difference density plots of the Fe (A–C) and Al (D and E) systems. (A and D) Top views. (B and E) Side views. (C and F) Front views. Contours are drawn on a linear scale from -0.65 to $0.65\text{ }e/\text{\AA}^3$ for the Fe system, and from -0.20 to $0.65\text{ }e/\text{\AA}^3$ for the Al system. The red, purple, and yellow colors represent Fe, Al, and C atoms as depicted in Figure 2A.

particular to the sp^2 dangling bonds of carbon. Consequently, the magnetic moment of the Fe_{13} nanoparticle is reduced from $44\text{ }\mu_{\text{B}}$ for the isolated structure to $36\text{ }\mu_{\text{B}}$ for the adsorbed Fe system. According to Chan et al.,⁵⁵ spin polarized electrons in an isolated transition metal such as Ti are transferred to less polarized graphene states when the atom is adsorbed on graphene. Upon Fe and Ti transition metal adsorption on perfect graphene,⁵⁵ the magnetic moments of Fe and Ti atoms are reduced from 4.00 to $2.03\text{ }\mu_{\text{B}}$ and 4.00 to $3.41\text{ }\mu_{\text{B}}$, respectively. Considering the magnetic moment reduction of Fe_{13} in the current study and the charge difference density analysis, it is likely that charge is transferred from Fe_{13} nanoparticle to defective graphene.

Figure 6B (Fe₁₃ system) shows that the majority of the charge is depleted from the vicinity of bound Fe, indicating that the charge is transferred from bound Fe to the neighboring carbons near the vacancy; however, in the case of the Al₁₃ system of Figure 6E, relatively weak charge depletion at the vicinity of bound Al is observed. The weak charge depletion of the Al-defective graphene system is caused by an underestimation of the charge density of isolated Al₁₃ since the isolated Al₁₃ structure used in the charge difference density plot is significantly more distorted and expanded compared to its optimized structure in the gas phase. In the charge difference density analysis and from eq 3, structures of isolated adsorbate and substrate are directly obtained from an optimized adsorbate–substrate system, so that the isolated adsorbate and substrate structures used in the charge difference density analysis can be different from their optimized structures in the gas phase when the geometry of an adsorbate is significantly distorted upon adsorption.

To quantitatively compare transferred electrons between the Fe and Al nanoparticles and defective graphene, Bader charge analyses have also been carried out. Table 2 indicates the excess charges of the Fe₁₃ and Al₁₃ systems over isolated nanoparticle and defective graphene for atoms labeled in Figure 3B. Bader charge analysis reveals large negative excess charges on the bound Fe and Al atoms (atom 1) of -0.47 and $-1.72e$, respectively, while large positive excess charges on the neighboring carbon atoms (C1, C2, and C3) near the vacancy site. This indicates that charges are transferred from the bound Fe and Al atoms to

Table 2. The Excess Bader Charge (in units of e) over the Isolated Nanoparticle and Defective Graphene for Atoms Labeled in Figure 3B

| | excess charge | | d-band center of Fe (before/after) |
|---------------------------------|---------------|-----------|---------------------------------------|
| | Fe system | Al system | |
| atom 1 | -0.47 | -1.72 | $-1.28/-1.48$ |
| atom 2 | 0.10 | -0.14 | $-1.30/-1.27$ |
| atom 3 | -0.29 | 0.07 | $-1.28/-1.14$ |
| atom 4 | -0.23 | -0.45 | $-1.28/-1.03$ |
| atom 5 | -0.11 | -0.19 | $-1.28/-1.03$ |
| atom 6 | 0.01 | -0.02 | $-1.28/-1.14$ |
| atom 7 | -0.01 | -0.05 | $-1.28/-1.08$ |
| atom 8 | -0.01 | -0.05 | $-1.28/-1.06$ |
| atom 9 | 0.01 | -0.07 | $-1.28/-1.10$ |
| C1 | 0.18 | 0.40 | |
| C2 | 0.13 | 0.86 | |
| C3 | 0.15 | 0.88 | |
| total (+) on all C ^a | 3.15 | 4.45 | |
| total (−) on all C | -1.58 | -1.36 | |
| total (+) on NP ^b | 0.12 | 0.12 | |
| total (−) on NP | -1.70 | -3.21 | |
| net on all C | 1.57 | 3.08 | |

^aTotal positive excess charge on defective graphene. ^bTotal positive excess charge on nanoparticles.

defective graphene. Table 2 also summarizes the total positive and negative excess charges on defective graphene and localized excess charges on C1, C2, and C3 atoms. Although the total negative excess charges on the defective graphene sites of the Fe ($-1.58e$) and Al ($-1.36e$) adsorbed systems are similar to each other, the total positive excess charge of the Fe system ($3.15e$) is smaller than that of the Al system ($4.45e$), resulting in net excess charges of defective graphene of 1.57 and $3.08e$ in the bound Fe and Al systems, respectively. The sum of positive

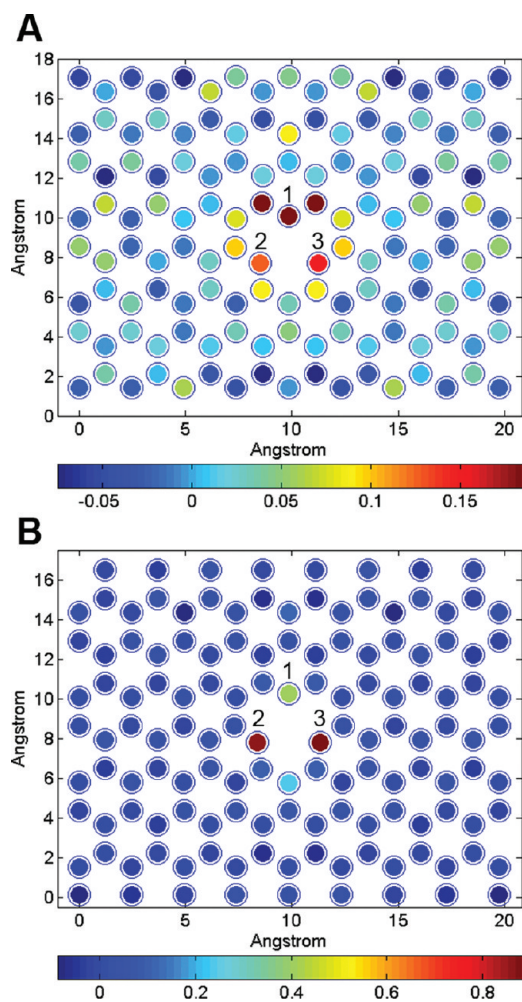


Figure 7. The excess Bader charge (in units of e) on the defective graphene of the (A) Fe_{13} system and (B) Al_{13} system over isolated nanoparticles and defective graphene.

excess charges of the C1, C2, and C3 atoms in the Fe and Al systems is 29 and 69% of the net excess charges of defective graphene, respectively. Comparing these values, we find that upon Fe_{13} adsorption, charge redistribution occurs throughout the entire surface of the defective graphene, while charge redistribution occurs on the localized site of defective graphene upon Al_{13} adsorption, as shown in Figure 7. Unlike Al with two s and one p valence electrons, the Fe_{13} d-states strongly hybridize with the defective graphene states to form covalent bonds, thereby significantly altering the electronic structure of defective graphene.⁵⁵ The charge redistribution of defective graphene in the Fe system may be understood by the Dewar–Chatt–Duncanson model,⁵⁶ in which filled π orbitals of carbon donate charge density to unoccupied d-orbitals of Fe, while other occupied d-orbitals back-donate into the empty π^* antibonding orbitals of carbon, as demonstrated in previous work in which the π –d orbital hybridization occurs on Pt-adsorbed carbon nanotubes⁵⁷ and Ti-doped fullerene.⁵⁸

Although charge transfer is both qualitatively and quantitatively described in the current study, using charge difference density and Bader charge analyses, a direct comparison of transferred charge between Fe and Al systems may not give useful insight for understanding nanoparticle adsorption on

defective graphene. This is because charge transfer is more applicable in the context of ionic bonding, while less relevant in the case of covalent bonding, such as the case of Fe due to shared charges in the covalent bond between adsorbate and substrate.⁵⁵ For ionic bonding systems, the work-function (Φ) and ionization potential (IP) are important electronic properties for evaluating charge transfer between adsorbate and substrate because both terms refer to energy required to remove electrons from an adsorbate–substrate system. Although work-function changes are not always governed by the sign and quantity of adsorbate-induced charge transfer,⁵⁹ charges are generally more likely transferred from adsorbates with lower Φ and IP. Chan et al.⁵⁵ correlate the calculated work-function shift relative to isolated perfect graphene ($\Delta\Phi$) with experimental ionization potentials (IP) for ionic and covalent bonding metals and find that adatoms with covalent bonding also follow the general trend of the $\Delta\Phi$ and IP correlation. Both Fe and Al show negative $\Delta\Phi$ (-1.02 for Fe and -1.18 eV for Al),⁵⁵ indicating that charges are transferred from Fe and Al to perfect graphene, with an IP of Fe and Al that is 7.90 and 5.99 eV, respectively.⁵⁵ Both $\Delta\Phi$ and IP of Fe and Al on perfect graphene suggest that charges are more likely to transfer from Al to perfect graphene rather than from Fe to perfect graphene. This trend supports the more negative net charge of Al_{13} ($-3.08\text{ }e$) in contrast to Fe_{13} ($-1.57\text{ }e$) on defective graphene as reported in the current study.

E. Enhancement of Catalytic Reactivity of Fe_{13} Nanoparticles. In addition to the PDOS evidence of the strong interaction between the nanoparticles and defective graphene, for transition metals the position of the d-band center is a good measure of the relative reactivity of a given surface.^{60,61} Although d-band theory has been primarily applied to determine the extent of surface reactivity within transition metals and their alloys, it is being applied in the current study as a measure to investigate the potential change in nanoparticle surface reactivity before and after adsorption on defective graphene. When materials of differing lattice constants are alloyed or layered, the d-band center can shift, based upon a modification in a given material's electronic structure. As the d-band center shifts, so do the antibonding orbitals. As antibonding orbitals shift higher in energy, they become more difficult to fill, leading to stronger binding of an adsorbate on a catalytic surface. For example, the strength of adsorption of CO and O atoms increases as the d-states of Au and Pt surfaces are shifted toward the Fermi level.⁶² In another study,⁶³ it was shown that CO binding on the $\text{FeCo}(100)$ alloy surface is stronger on the Co-terminated surface compared to the Fe-terminated surface and that the d-band center of the Co surface is closer to the Fermi level than that of the Fe surface. These examples show that the enhanced catalytic activities of metal surfaces can be proven by examining the d-band center shift. In the current study, the d-band center of the isolated Fe_{13} nanoparticle is -1.28 eV and shifts up to -1.13 eV after adsorption, indicating that the reactivity of the nanoparticle may be enhanced upon adsorption. Table 2 shows individual d-band centers of the Fe atoms in the nanoparticle labeled in Figure 3B, and all of the Fe atoms of the isolated Fe_{13} show the same d-band centers, i.e., -1.28 eV, except for the centered Fe2 atom (-1.30 eV) due to the symmetry of the icosahedral cluster. For adsorbed Fe_{13} , the d-band center of the bound Fe1 atom is the lowest (-1.48 eV) among the Fe atoms, even further away from the Fermi level than that of the isolated Fe_{13} due to the bond formation of Fe with the sp^2 dangling bonds of the carbon atoms of defective graphene. However, the remainder of the Fe

atoms show shifted d-band centers ranging from -1.03 to -1.27 eV. It may be useful to know for further catalytic studies which site on the adsorbed nanoparticle exhibits the highest catalytic reactivity. The highest d-band center is shown at Fe4 and Fe5 atoms in Figure 3B, -1.03 eV, followed by Fe8 (-1.06 eV), Fe7 (-1.08 eV), and Fe9 (-1.10 eV) atoms. Future work should include the investigation of these sites for potentially enhanced reactant uptake. However, it should be noted that if these sites bind a reactant too strongly, this is not favorable for intermediate formation and catalyst turnover; hence, a balance in the binding strength should be sought.

4. CONCLUSIONS

We demonstrate stable anchoring of Fe_{13} and Al_{13} nanoparticles on defective graphene by showing relatively strong adsorption energies of Fe_{13} (-6.98 eV) and Al_{13} (-3.84 eV) nanoparticles on the monovacancy defect site of graphene. Upon adsorption of the nanoparticles, the sp^2 dangling bonds of neighboring carbons near the vacancy site significantly contribute to anchoring the nanoparticles, so that the height of the neighboring carbon atoms increases up to 1.09 and 1.48 Å for Fe_{13} and Al_{13} systems, respectively, while lateral relaxation of the graphene lattice is not significant. PDOS analyses also support strong hybridization of the nanoparticles with the sp^2 dangling bonds of carbon. Charges are transferred mostly from the bound nanoparticles at the vacancy to defective graphene, and the net charge accumulations on defective graphene are 1.57 and $3.08e$ for the Fe and Al systems, respectively. Due to Fe_{13} d-states, charge redistribution of the defective graphene in the Fe system occurs throughout the entire surface of the defective graphene, while charge redistribution occurs only locally around the vacancy site upon Al_{13} adsorption. We also suggest enhanced catalytic reactivity of the Fe_{13} nanoparticles upon adsorption on defective graphene indicated from a d-band center shift closer to the Fermi level upon adsorption (from -1.28 to -1.13 eV).

■ ASSOCIATED CONTENT

5 Supporting Information. Adsorption configurations of B–B, B–A, T–B, T–A, and another type of A–B modes of Fe_{13} and Al_{13} nanoparticles on the monovacancy defective graphene. This material is available free of charge via the Internet at <http://pubs.acs.org>.

■ AUTHOR INFORMATION

Corresponding Author

*E-mail: wilcoxj@stanford.edu. Phone: (650) 724-9449. Fax: (650) 725-2099.

■ ACKNOWLEDGMENT

This work was supported by a grant from the Air Force Office of Scientific Research under grant number FA9550-09-1-0523. The computational resources were supported by the National Science Foundation through TeraGrid resources provided by TACC. The authors would like to acknowledge Dr. Shela Aboud for helpful discussions during the early stages of this work.

■ REFERENCES

- (1) Iijima, S. *Nature* **1991**, *354*, 56.
- (2) McAllister, M. J.; Li, J. L.; Adamson, D. H.; Schniepp, H. C.; Abdala, A. A.; Liu, J.; Herrera-Alonso, M.; Milius, D. L.; Car, R.; Prud'homme, R. K.; Aksay, I. A. *Chem. Mater.* **2007**, *19*, 4396.
- (3) Carlsson, J. M.; Scheffler, M. *Phys. Rev. Lett.* **2006**, *96*, 046806.
- (4) Boukhvalov, D. W.; Katsnelson, M. I. *Nano Lett.* **2008**, *8*, 4373.
- (5) Kudin, K. N.; Ozbas, B.; Schniepp, H. C.; Prud'homme, R. K.; Aksay, I. A.; Car, R. *Nano Lett.* **2008**, *8*, 36.
- (6) Hashimoto, A.; Suenaga, K.; Gloter, A.; Urita, K.; Iijima, S. *Nature* **2004**, *430*, 870.
- (7) Lee, G.-D.; Wang, C. Z.; Yoon, E.; Hwang, N.-M.; Kim, D.-Y.; Ho, K. M. *Phys. Rev. Lett.* **2005**, *95*, 205501.
- (8) Wang, H. L.; Robinson, J. T.; Diankov, G.; Dai, H. J. *J. Am. Chem. Soc.* **2010**, *132*, 3270.
- (9) Simon, P.; Gegotsi, Y. *Nat. Mater.* **2008**, *7*, 845.
- (10) Medasani, B.; Vasiliev, I. *Surf. Sci.* **2009**, *603*, 2042.
- (11) Parks, E. K.; Weiller, B. H.; Bechthold, P. S.; Hoffman, W. F.; Nieman, G. C.; Pobo, L. G.; Riley, S. J. *J. Chem. Phys.* **1988**, *88*, 1622.
- (12) Diéguez, O.; Alemany, M. M. G.; Rey, C.; Ordejón, P.; Gallego, L. *J. Phys. Rev. B* **2001**, *63*, 205407.
- (13) Rollmann, G.; Entel, P.; Sahoo, S. *Comput. Mater. Sci.* **2006**, *35*, 275.
- (14) Ma, Q. M.; Xie, Z.; Wang, J.; Liu, Y.; Li, Y. C. *Solid State Commun.* **2007**, *142*, 114.
- (15) Šljivančanin, Ž.; Pasquarello, A. *Phys. Rev. Lett.* **2003**, *90*, 247202.
- (16) Xie, Y.; Blackman, J. A. *Phys. Rev. B* **2002**, *66*, 085410.
- (17) Bockmon, B. S.; Pantoya, M. L.; Son, S. F.; Asay, B. W.; Mang, J. T. *J. Appl. Phys.* **2005**, *98*, 064903.
- (18) Sutton, G. P. *Rocket Propulsion Elements*; John Wiley & Sons: New York, 1992.
- (19) Sakurai, M.; Watanabe, K.; Sumiyama, K.; Suzuki, K. *J. Chem. Phys.* **1999**, *111*, 235.
- (20) Lian, L.; Su, C. X.; Armentrout, P. B. *J. Chem. Phys.* **1992**, *97*, 4072.
- (21) Bobadova-Parvanova, P.; Jackson, K. A.; Srinivas, S.; Horoi, M. *Phys. Rev. B* **2002**, *66*, 195402.
- (22) Rollmann, G.; Gruner, M. E.; Hucht, A.; Meyer, R.; Entel, P.; Tiago, M. L.; Chelikowsky, J. R. *Phys. Rev. Lett.* **2007**, *99*, 083402.
- (23) Boukhvalov, D. W.; Katsnelson, M. I. *J. Phys.: Condens. Matter* **2009**, *21*, 344205.
- (24) Sanz-Navarro, C. F.; Åstrand, P. O.; Chen, D.; Ronning, M.; van Duin, A. C. T.; Jacob, T.; Goddard, W. A. *J. Phys. Chem. A* **2008**, *112*, 1392.
- (25) Kresse, G.; Hafner, J. *Phys. Rev. B* **1993**, *47*, 558.
- (26) Kresse, G.; Hafner, J. *Phys. Rev. B* **1994**, *49*, 14251.
- (27) Kresse, G.; Furthmüller, J. *Phys. Rev. B* **1996**, *54*, 11169.
- (28) Kresse, G.; Furthmüller, J. *Comput. Mater. Sci.* **1996**, *6*, 15.
- (29) Blöchl, P. E. *Phys. Rev. B* **1994**, *50*, 17953.
- (30) Kresse, G.; Joubert, D. *Phys. Rev. B* **1999**, *59*, 1758.
- (31) Perdew, J. P.; Burke, K.; Ernzerhof, M. *Phys. Rev. Lett.* **1996**, *77*, 3865.
- (32) Neugebauer, J.; Scheffler, M. *Phys. Rev. B* **1992**, *46*, 16067.
- (33) Makov, G.; Payne, M. C. *Phys. Rev. B* **1995**, *51*, 4014.
- (34) Monkhorst, H. J.; Pack, J. D. *Phys. Rev. B* **1976**, *13*, 5188.
- (35) Methfessel, M.; Paxton, A. T. *Phys. Rev. B* **1989**, *40*, 3616.
- (36) Gerber, I. C.; Krasheninnikov, A. V.; Foster, A. S.; Nieminen, R. M. *New J. Phys.* **2010**, *12*, 113021.
- (37) Isvoranu, C.; Ahlund, J.; Wang, B.; Ataman, E.; Martensson, N.; Puglia, C.; Andersen, J. N.; Bocquet, M. L.; Schnadt, J. *J. Chem. Phys.* **2009**, *131*, 214709.
- (38) Ma, Y.; Lehtinen, P. O.; Foster, A. S.; Nieminen, R. M. *New J. Phys.* **2004**, *6*, 68.
- (39) Singh, R.; Kroll, P. *J. Phys.: Condens. Matter* **2009**, *21*, 196002.
- (40) Kokalj, A. *Comput. Mater. Sci.* **2003**, *28*, 155.
- (41) Bader, R. F. W. *Chem. Rev.* **1991**, *91*, 893.
- (42) Henkelman Group; The University of Texas at Austin, <http://theory.cm.utexas.edu/henkelman/research/bader/> (accessed Jan, 2011).
- (43) Tang, W.; Sanville, E.; Henkelman, G. *J. Phys.: Condens. Matter* **2009**, *21*, 084204.

- (44) Yazyev, O. V.; Helm, L. *Phys. Rev. B* **2007**, *75*, 125408.
- (45) El-Barbary, A. A.; Telling, R. H.; Ewels, C. P.; Heggie, M. L.; Briddon, P. R. *Phys. Rev. B* **2003**, *68*, 144107.
- (46) Yang, X. M.; Xia, H. H.; Qin, X. B.; Li, W. F.; Dai, Y. Y.; Liu, X. D.; Zhao, M. W.; Xia, Y. Y.; Yan, S. S.; Wang, B. Y. *Carbon* **2009**, *47*, 1399.
- (47) Thrower, P. A.; Mayer, R. M. *Phys. Status Solidi A* **1978**, *47*, 11.
- (48) Nelayev, V. V.; Mironchik, A. I. *Mater. Phys. Mech.* **2010**, *9*, 26.
- (49) Rollmann, G.; Sahoo, S.; Entel, P. *Phys. Status Solidi A* **2004**, *201*, 3263.
- (50) Zhou, M.; Zhang, A. H.; Dai, Z. X.; Zhang, C.; Feng, Y. P. *J. Chem. Phys.* **2010**, *132*, 194704.
- (51) Akola, J.; Hakkinen, H. *Phys. Rev. B* **2006**, *74*, 165404.
- (52) Li, Y. F.; Zhou, Z.; Yu, G. T.; Chen, W.; Chen, Z. F. *J. Phys. Chem. C* **2010**, *114*, 6250.
- (53) Cabrera-Sanfelix, P. J. *Phys. Chem. A* **2009**, *113*, 493.
- (54) Liu, Y.; Wilcox, J. *Environ. Sci. Technol.* **2011**, *45*, 809.
- (55) Chan, K. T.; Neaton, J. B.; Cohen, M. L. *Phys. Rev. B* **2008**, *77*, 235430.
- (56) Leigh, G. J.; Winterton, N. *Modern Coordination Chemistry-The Legacy of Joseph Chatt*; Royal Society of Chemistry: Cambridge, United Kingdom, 2002.
- (57) Xiao, H.; Li, S. H.; Cao, J. X. *Chem. Phys. Lett.* **2009**, *483*, 111.
- (58) Guo, J.; Liu, Z.; Liu, S.; Zhao, X.; Huang, K. *Appl. Phys. Lett.* **2011**, *98*, 0231107.
- (59) Leung, T. C.; Kao, C. L.; Su, W. S.; Feng, Y. J.; Chan, C. T. *Phys. Rev. B* **2003**, *68*, 195408.
- (60) Hammer, B.; Nørskov, J. K. *Surf. Sci.* **1995**, *343*, 211.
- (61) Hammer, B.; Nørskov, J. K. Theoretical surface science and catalysis - Calculations and concepts. In *Advances in Catalysis*; Academic Press Inc.: San Diego, 2000; Vol. 45; p 71.
- (62) Jiang, T.; Mowbray, D. J.; Dobrin, S.; Falsig, H.; Hvolbaek, B.; Bligaard, T.; Norskov, J. K. *J. Phys. Chem. C* **2009**, *113*, 10548.
- (63) Rochana, P.; Wilcox, J. *Surf. Sci.* **2011**, *605*, 681.